Check for updates

Narrowing of band gap and decrease in dielectric loss in La₁₋ₓSrₓMnO₃ for x = 0.0, 0.1, and 0.2 manganite nanoparticles

Akhtar Ali[1]*, Wiqar H. Shah[1]*, Zakir Ullah[1], Shaheryar Malik[1], Muhammad Rauf[1], Sameh Askar[2]*, Naveed Imran[3,4] and Hijaz Ahmad[5]

[1]Department of Physics, Faculty of Sciences, International Islamic University, Islamabad, Pakistan, [2]Department of Statistics and Operations Research, College of Science, King Saud University, Riyadh, Saudi Arabia, [3]HITEC Colleges, HIT Taxila Cantt, Rawlpindi, Pakistan, [4]Institute of Space Technology, Islamabad, Pakistan, [5]Section of Mathematics, International Telematic University Uninettuno, Corso Vittorio Emanuele II, Roma, Italy

Polycrystalline compounds of lanthanum strontium manganite ($La_{1-x}Sr_xMnO_3$, LSMO) are widely used in electronic storage devices due to their minimal losses and electronic charge transport properties. In this study, we investigated how varying substitutions of Sr^{2+} for values of $x = 0.0$, 0.1, and 0.2 affected the tuning of the optical band gap and dielectric losses in $La_{1-x}Sr_xMnO_3$ nanoparticles. Synthesized samples were structurally analyzed via X-ray diffraction. A rhombohedral $R\bar{3}c$ crystal structure was confirmed for all prepared samples; crystallite size ranging from 15 nm to 20 nm was estimated along with other lattice parameters. Polygonal or hexagonal-like morphology was revealed by field emission scanning electron microscopy, with a moderate size distribution of nanoparticles affected by thinner grain boundaries in doped LSMO. Energy dispersive spectroscopy was employed to confirm the elemental composition of each compound, and the infrared spectrum indicated bonding in the fingerprint region It was observed that there was a significant reduction in the optical band gap, which was measured using ultraviolet spectrometer absorption data. The band gap decreased from 4.34 eV to 4.11 eV. This reduction was found to be related to the difference in refractive index, which was calculated using both Moss and Herve–Vandamme relations. In parallel, frequency-dependent dielectric analysis revealed that frequency was proportional to the increase in Sr content, inversely affecting dielectric loss. Moreover, the AC conductivity of the prepared samples increased with the rise in Sr content, as described by Johnscher's universal power law in the region of high frequency.

KEYWORDS

LSMO nanoparticles, co-precipitation, optical band gap, dielectric constant, dielectric loss, ac conductivity

1 Introduction

In recent years, research motivated by the development of renewable energy resources has become a popular area for scientists. The use of natural energy resources creates a pollution-free environment and contributes less to climate change as compared to fossil fuels. Numerous materials are fabricated to convert these energy resources into useful

electrical energy. For this reason, extensive research has been conducted on lanthanum-based ABO_3-type perovskite oxide materials due to their diverse range of applications in many electrical and magnetic storage devices. In ABO_3-type perovskite, A represents rare earth or alkaline earth positive cation metals and B denotes transition metal cations; their combined sum is 6, as in $A^{3+}B^{3+}O_3$, $A^{2+}B^{4+}O_3$, or $A^{1+}B^{5+}O_3$. Lanthanum manganite ($LaMnO_3$) nanoparticles exhibit unique optical and electrical properties and are widely used in many applications such as LiO_2 batteries, supercapacitors, photocatalytic activity, and sustainable dye-synthesized solar cells (Hernández et al., 2015; Li et al., 2018; Shafi et al., 2018; Özkan et al., 2021). Existing studies have reported that high-specific-surface-area $LaMnO_3$ nanoparticles are associated with very high catalytic activity in the oxygen reduction reaction (ORR) and oxygen evolution reaction (OER) due to the creation of oxygen vacancies in the Mn^{3+}-O^{2-}-Mn^{4+} network (Li et al., 2018; Miao et al., 2020; Yan et al., 2020). The Jahn–Teller distortion in the octahedral symmetry of MnO_6 due to substitution on either the A or the B site in the $LaMnO_3$ system causes transitions from Mn^{3+} to Mn^{4+} ions, thereby enhancing the chemical stability, colossal magnetoresistance, nitrogen monoxide (NO) absorption capacity, and pseudocapacitive performance of perovskite materials (Shafi et al., 2018; Hu et al., 2019; Flores-Lasluisa et al., 2022). We can control particle size, electrical conductivity, optical band gap, and dielectric constant by partially substituting the divalent cation, such as Ca^{2+}, Sr^{2+}, Ba^{2+}, or Mg^{2+} (Solopan et al., 2012; Zhong et al., 2013; Afify et al., 2021), with an La^{3+} ion on the A site in $La_{1-x}A_xMnO_3$ perovskites.

Over the course of a few years, it has been observed that partially substituted lanthanum magnetite ($La_{1-x}A_xMnO_3$) nanoparticles undergo electric polarization to determine the permittivity spectrum; based on this spectrum, this material is competitive in several applications due to its extremely high static dielectric constant (specifically, on the order of 105) (Assoudi et al., 2018; Mleiki et al., 2020). Doping with alkaline earth metals, such as Sr^{2+}, enhances the material's overall optical and dielectric characteristics. Tripathi et al. (Naseem Siddique et al., 2019) have reported that Sr reduces defects and improves the optical spectra of NiO nanoparticles. Du Huiling et al. (Arshad et al., 2020) revealed that dielectric losses are reduced upon Sr^{2+} doping in BST ceramics. Kandil et al. (Turky and Kandil, 2013) observed a significant increase in dielectric constant with the use of a higher Sr^{2+} molar ratio in BST nanoparticles. Transition metals, such as manganese (Mn), play a vital role in charge transport when it undergoes transition via partial replacement of Sr^{2+} (1.44 Å) with La^{3+} (1.36 Å) (Turky et al., 2016), improving electrical properties that are connected to dielectric losses in the desired material. Typically, tunneling and hooping processes can demonstrate the movement of these charge carriers (Hizi et al., 2022). In polycrystalline material, at high frequency, charge carriers move from one localized state to another across grain boundaries through a process known as hooping, which can reduce the defect density and contribute to an increase in the AC conductivity of the material (Mohanty et al., 2020a). It has been reported that, in an external electric field, charge carriers build up at grain boundaries and cause polarization in the material, thereby increasing the dielectric constant and overall electrical AC conductivity of doped material (Mohanty et al., 2020a; Mohanty et al., 2020b). Ali Omar Turky et al. prepared LSM nanoparticles for values of $x = 0.2, 0.5,$

and 0.8 using precipitation (Turky et al., 2016) and citrate precursor (Turky et al., 2017) techniques, and reported observing increases in the optical band gap with a decrease in dielectric constant for higher values of x. According to Andreja Žužić et al. (Žužić et al., 2022), LSM nanoparticles prepared by the co-precipitation method possess higher electrical conductivity. Sandhya Suresh et al. (Sandhya et al., 2023) synthesized a series of LSM nanoparticles for values of $x = 0.0, 0.3, 0.5, 0.7$ by the combustion method and observed band gap increases with a decrease in the refractive index and dielectric losses. The main highlight of this work was the $x = 0.7$ sample; the authors noted a significant increase in dielectric constant with minimal dielectric losses, which may be attributable to large grain boundaries with comparatively more strain produced by Mn^{4+} ions on lattice sites. Extensive research has been conducted on LSM nanoparticles, as a result of which the research gap has been diminished; however, here we report a decrease in losses with band gap in a series of $La_{1-x}Sr_xMnO_3$ stable nanoparticles for $x = 0.0, 0.1, 0.2$, synthesized by the precipitation method.

To avoid low conducting $SrZrO_3$ phase formation, we utilized molar ratios of Sr ion of only 0.0, 0.1, and 0.2 in the $La_{1-x}Sr_xMnO_3$ lattice for relatively a high conducting phase. It has been reported that samples prepared via the precipitation technique have higher conductivity, recorded as 0.176 $\Omega^{-1} \cdot cm^{-1}$ at room temperature for 20% Sr^{2+} concentration, which is comparable to the conductivity of silicon (Žužić et al., 2022). The hooping mechanism at the octahedral site in this $La_{1-x}Sr_xMnO_3$ system indicates that the tuning of optoelectrical properties, including optical band gap, refractive index, frequency-dependent dielectric constant, dielectric losses, and AC conductivity, is strongly influenced by degrees of substitution, lattice mismatch, and grain size.

2 Experimental details

2.1 Materials

Chemicals with purity levels of 99.99% were utilized in the experiment, including strontium chloride hexahydrate [$SrCl_2.6H_2O$], manganese acetate tetrahydrate [$C_4H_6 MnO_4.4H_2O$], and lanthanum (III) nitrate hexahydrate [$La (NO_3)_3.6H_2O$]. As a precipitating agent, sodium hydroxide (NaOH) was also made available by Sigma-Aldrich. The chemicals were all utilized as procured directly from the supplier without any additional purification.

2.2 Sample preparation

To obtain LSMO nanoparticles for both undoped and Sr-doped samples, the co-precipitation method was utilized. Chemicals including strontium chloride hexahydrate [$SrCl_2.6H_2O$], manganese acetate tetrahydrate [$C_4H_6 MnO_4.4H_2O$], and lanthanum (III) nitrate hexahydrate [$La (NO_3)_3.6H_2O$] were used in the experiment. These chemicals were dissolved in 300 mL of deionized water in the proportions of (1-x) (La $(NO_3)_3.6H_2O$):x ($SrCl_2.6H_2O$): ($C_4H_6 MnO_4.4H_2O$) for (0.0 ≤ x ≤ 0·2), with a 5-g sample of each. The pH was adjusted to 8.5 through addition of 50 mL of a 1M NaOH solution progressively, with constant

stirring, for 2 hours at 80 °C until black precipitates were obtained. The precipitates were cleaned of contaminants by centrifuging for 10 minutes; they were rinsed with distilled water each time. To obtain maximum yield, a filtration technique with Whatman filter paper was employed, and the precipitates were dried at 100°C for 5 h to obtain a pure solid phase. The final yield, LSMO powder, was annealed in a tube furnace for 10 h at 600°C. The same procedure was used to obtain Sr-doped specimens. The prepared samples were labeled La$_{1-x}$Sr$_x$MnO$_3$ for x = 0.0, 0.1, 0.2 nanoparticles.

2.3 Characterization techniques for LSMO powder

Advanced nanotechnology methods were utilized to characterize the atomic behavior of powder LSMO nanoparticles. A diffractometer system (XPERT-3 Malvern Panalytical) was utilized to investigate crystallographic manipulation over a wide angular region ($5^0 \leq 2\theta \leq 100^0$) with a counting rate of 3 s per step (size = 0.02^0) and XRD (Cu-k alpha radiation) of a specific wavelength, approximately 1.5406 Å. The shape of particles was determined at the nanoscale using a high-resolution imaging device, the SEM-VEGA 3 TESKAN field emission scanning electron microscope, with energy-dispersive X-ray spectroscopy (EDX) for elemental identification in the material. For confirmation of bonds and molecular vibration at a frequency range of 400–4,000 cm^{-1}, the IRTracer-100 apparatus was used. A UV-visible SPECORD 200 PLUS spectrometer was used to analyze the optical properties of the materials. Finally, the AC conductivity and dielectric properties of the samples were evaluated using a gold terminal pellet (1 kHz–2 MHz) impedance analyzer.
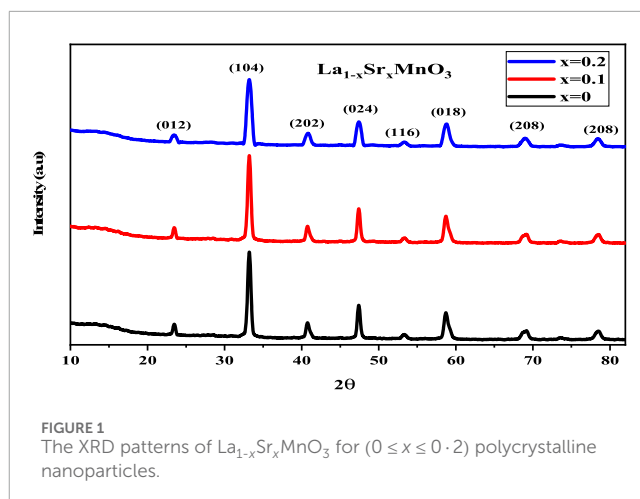
3 Results and discussion

3.1 Structural properties

The X-ray diffraction (XRD) profiles of all prepared samples revealed their composition of pure La$_{1-x}$Sr$_x$MnO$_3$ ($0 \leq x \leq 0 \cdot 2$) polycrystalline nanocrystals. These samples were synthesized using the co-precipitation method, then calcined at 600 °C for 10 h, and subsequently cooled to room temperature, as shown in Figure 1. The XRD patterns for all compositions indicated a monophasic crystal structure without any further impurities. All samples possess a rhombohedral ($R\,\overline{3}c$ – space group) crystal structure, with their lattice constants confirmed by the Xpert high score program with reference JCPDS card numbers of 01-088-0126, 01-089-0647, and 01-089-0648 for each composition of Sr^{2+}; this appears to be consistent with previously published data (Žužić et al., 2022).

To ensure sample phase purity, step scanning was performed at room temperature across the angular range 22.9° < 2 theta <68.6°. In Figure 1, peaks are indexed according to the electron density in the material at different diffraction angles.

The average crystallite size (D) was determined using Debye-Scherer's equation:

$$D = \frac{0.9\lambda}{\beta\cos\theta},$$ (1)

FIGURE 1
The XRD patterns of La$_{1-x}$Sr$_x$MnO$_3$ for ($0 \leq x \leq 0 \cdot 2$) polycrystalline nanoparticles.

where D represents the crystallite size, λ the wavelength of X-rays, θ the Bragg diffraction angle, and β the full width at half maximum (FWHM) of the diffraction peak (Wang et al., 2022; Ali Akhtar et al., 2023). The average crystallite size ranged between 15 and 20 nm, clarifying the crystallinity of the synthesized samples. The lattice constant obtained indicated anisotropic behavior with unit cell volume, which may be attributed to two main factors. First, the substitution of a relatively larger ion Sr^{2+} (1.44 Å) for coordination number 12 could have caused a portion of the Mn^{3+} ions to oxidize to Mn^{4+} ions, which have smaller ionic radii (Žužić et al., 2022). This oxidation could result in a contraction of the unit cell. Second, the existence of vacancies at oxygen sites might also have contributed to the reduction of electrostatic forces, leading to a decrease in unit cell volume. The lattice constants obtained for rhombohedrals with a hexagonal morphology (Manohar and Krishnamoorthi, 2017) are related to the unit cell volume given by Eq 2:

$$V_{cell} = \frac{\overline{\sqrt{3}}}{2}\,a^2c,$$ (2)

where a and c are lattice constants (Shkir et al., 2020a). It has been noticed that the presence of Sr^{2+} in host lattice La$_{1-x}$Sr$_x$MnO$_3$ decreases the dislocation density (defects per unit volume); this can be defined in terms of interims of crystallite size as:

$$\delta = \frac{1}{D^2}$$ (3)

The outcomes of Eq 3 (Chandekar et al., 2021b) confirmed that the crystallinity of the desired samples increased with a decrease in defects from 0.0044 to 0.0025, which makes them more suitable for storage applications. The macro strain, X-ray density, and specific surface area were also estimated to identify the influence of dopant atoms on their optoelectrical properties; this is discussed in later sections. Hence, Eqs 4–6 were used to determine the micro-strain, X-ray density, and specific surface area expressed as follows:

$$Micro - strain, (\varepsilon) = \frac{\beta\cot\theta}{4}, [43]$$ (4)

$$\rho_{x-ray} = \frac{ZM}{V_{cell}\text{x}N_A}, [41]$$ (5)

and

$$S = 6000/\rho * D, [42] \qquad (6)$$

In Eq 5, ρ_{x-ray} denotes the X-ray density, depending on molecular weight, coordination number, Avogadro's number, and unit cell volume. All findings in terms of crystallographic data are tabulated in Table 1. The Jahn–Teller distortion in MnO_6 plays a central role in modifying the lattice parameters, which enhances the electrical properties due to offering more vacancies as a result of Mn^{3+} to Mn^{4+} transitions.

3.2 Morphological studies

Field emission scanning electron microscopy (FESEM) was utilized to investigate the surface morphology of all prepared samples. No additional contaminants were observed in SEM images, as shown in Figure 2A–C. The XRD results exhibited strong agreement: with no extra phases, all LSMO-prepared nanoparticles for x = 0.0, 0.1, and 0.2 annealed at 600°C for 10 h confirmed the hexagonal-like morphology of the nanoparticles. A high potential of approximately 10.0 kV electrons was employed to capture images using backscattered electrons at resolutions of 500 nm and 200 nm, illustrated with histograms in Figure 2A–C. It can be seen that, in the case of 0.2 concentration of Sr^{2+} ion content, the particles were agglomerated faceted powders. A higher concentration of Sr^{2+} ion created more defects in the crystal structure via oxidization of Mn^{3+}/Mn^{4+} transitions, leading to a more conductive nature. The average particle or grain size distribution is shown for all LSMO compounds, and the moderate ranges of particles in SEM images are displayed in histograms. The particle sizes of all reported samples are listed in Table 2.

A simple statistical relation was utilized to calculate average particle size from the corresponding histograms: $\langle D \rangle = \frac{\sum midpoint \times frequency}{\sum frequency}$. Here $\langle D \rangle$ is the average diameter of each particle. A significant increase in the average particle or grain size $\langle D \rangle$ was observed. This means that the partial substitution of a larger ion Sr^{2+} (1.44 Å) with the smaller La^{3+} (1.36 Å) causes a reduction in lattice constant with a specific surface area of prepared nanoparticles, as mentioned in Table 1. According to Table 1, crystallite size increased with a decrease in defects/voids in a material; as a result of this, porosity was reduced alongside enhancement of conductivity, which is beneficial in enabling photovoltaic devices to store more electrical energy. The increase in particle size may be attributed to small grain boundaries, at

which the hooping of charge carriers plays a significant role in surface effects that make these materials promising for a variety of applications in SOFCs and many other electronic storage devices.

3.3 Compositional analysis

Energy-dispersive X-ray (EDX) spectra offer proof of the stoichiometry of the nominal composition. Quantitative energy-dispersive X-ray spectroscopy was used to determine the chemical composition of the synthetic $La_{1-x}Sr_xMnO_3$ (x = 0.0, 0.1, 0.2) samples, as shown in Figure 3A–C.

The elements La, Sr, Mn, and O were present in the synthetic samples, according to the EDX spectrum. Figure 3A–C illustrates the presence of peaks for lanthanum, manganese, oxygen, and strontium, illustrating the phase purity and elemental composition. There was no additional peak for impurities.

The initial values utilized during synthesis and the atomic weight percentages of elements used during synthesis as obtained from the EDX spectrum were in good accord. The weights and atomic percentages of the samples are shown in Table 3. Nanoparticles that were created had an excess of oxygen and a nearly stoichiometric composition (Jadhav et al., 2015).

3.4 FTIR analysis

Using IRTracer-100, functional groups located in prepared samples in the 400–4,000 cm^{-1} range were identified. The Fourier transform infrared (FTIR) spectroscopy spectra of each sample are shown in Figure 4. Six oxygen atoms were positioned around one Mn atom in the MnO_6 structure, which had perfect octahedral symmetry. IR activity was present in only two of the six vibrational modes. These IR band positions matched well with those reported in the literature (Hassan et al., 2020). The bending modes of Mn-O around 465 and 477 cm^{-1} can be attributed to a change in the Mn-O-Mn bond angle, as observed, whereas stretching vibrations in Mn-O-Mn can be ascribed to the wavenumber between 690 and 706 cm^{-1}. Bending and stretching vibrations may be due to a change in bond angle and internal motion or a change in the length of the Mn-O-Mn molecule.

Transmission peaks of Mn-O-Mn stretching are shifted toward a lower wave number, while the bending vibrations of Mn-O-Mn are displaced to a higher one, according to the energy relation represented by Eq 7. The change in the bond length and angle under the influence of ionic defects in the crystal lattice brought on by the

TABLE 1 Lattice constants, crystallite size, unit cell volume, specific surface area, X-ray density, dislocation density, and micro-strain for $La_{1-x}Sr_xMnO_3$.

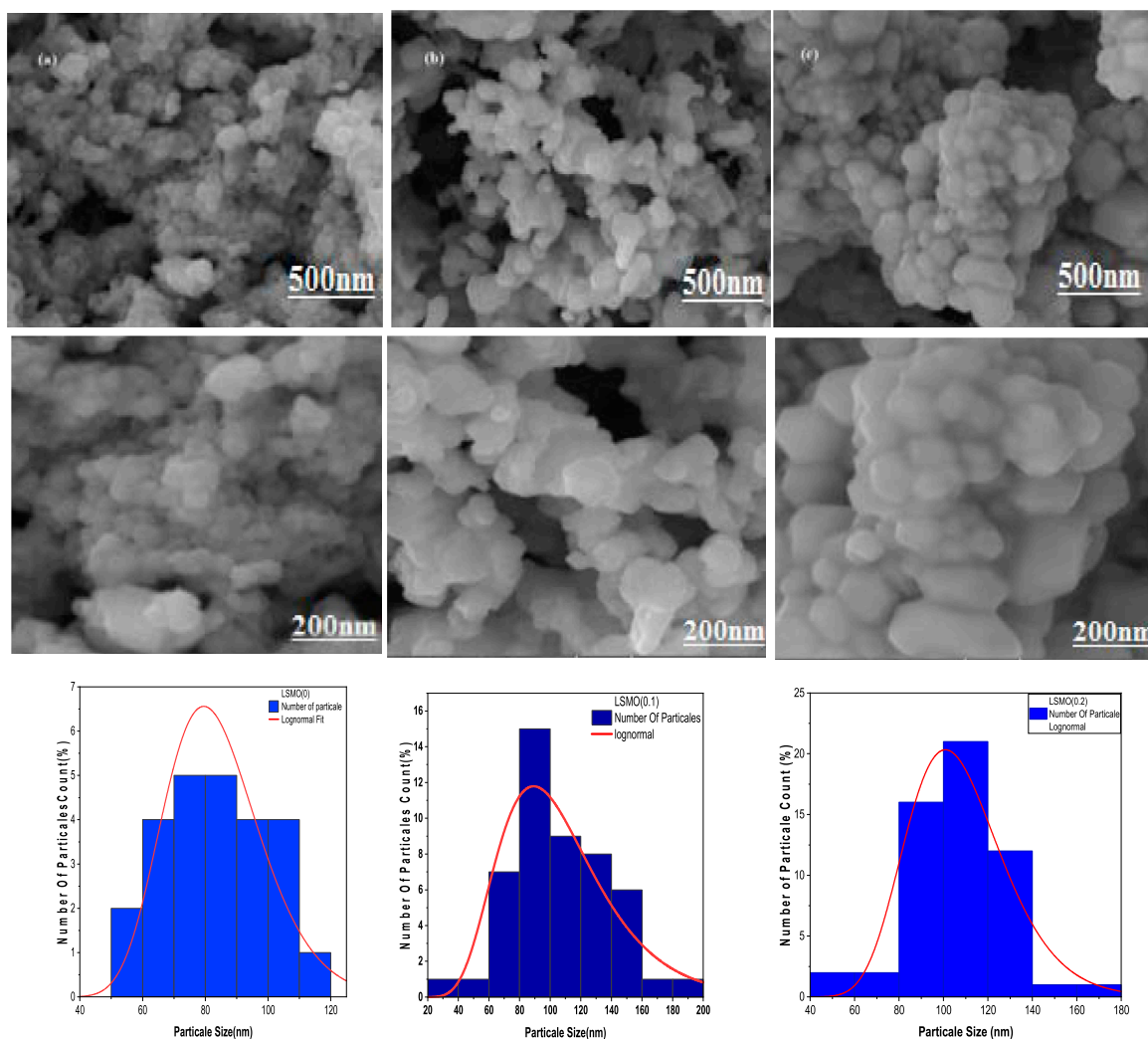| $La_{1-x}Sr_xMnO_3$ Samples for x =	Lattice constant (a = b) (Å)	Lattice constant (c) (Å)	Crystallite size (nm)	Unit cell volume	S (cm^2/g)	ρ (g/cm^3)	$\delta_{av} \times 10^{-3}$ ($1/nm^2$)	$\varepsilon_{av} \times 10^{-3}$
0.0	5.4951	13.3030	15	347.88	57.80	6.92	0.0044	2.238
0.1	5.5242	13.3481	15.9	352.76	56.49	6.68	0.0039	3.091
0.2	5.5172	13.3590	20	352.16	45.80	6.55	0.0025	2.572

FIGURE 2
(A–C): FESEM images and histograms of La$_{1-x}$Sr$_x$MnO$_3$.

TABLE 2 The average particle or grain size of LSMO nanoparticles.

La$_{1-x}$Sr$_x$MnO$_3$ samples for x =	$\langle D \rangle$ (nm)
0.0	87 nm
0.1	106 nm
0.2	119 nm

substitution ratio Sr^{2+}/La^{3+} leads to a transition from Mn^{3+} to the smaller Mn^{4+} ion.

$$E = \frac{hc}{\lambda} \qquad (7)$$

where c represents the photon's speed, E the photon's energy, h Planck's constant, and λ the wavelength. We may observe the absorbance peak of the La-Sr bond at 898 cm^{-1} as a result of substitution of Sr into pure LaMnO$_3$. Environmental CO$_2$

causes an additional peak around 1,496, 1,499, 1,689, 1,552, 1,556, and 1759 cm^{-1}. The peak is present at approximately 2,985-299 cm^{-1} due to surface-adsorbed water on LSMO particles, as well as approximately 2,347–2,470 cm^{-1} in ambient circumstances (McBride et al., 2016).

3.5 Optical measurements

The influence of Sr^{2+} on the optical and charge transport properties of La$_{1-x}$Sr$_x$MnO$_3$ for x = 0.0, 0.1, and 0.2 nanostructures can be discussed in terms of optical band gap and refractive index. The absorption spectrum of LSMO nanoparticles in an ultraviolet (UV) region (200-340) nm is shown in Figure 5. All samples possessed a good absorption edge in the UV range, which can be ascribed to the inorganic nature of LSMO compound; typically, direct and forbidden transitions are responsible for such weak absorption peaks around 280 nm (Naseem Siddique et al., 2019). It can be observed that, as a result of increasing Sr^{2+} content from 0.1 to
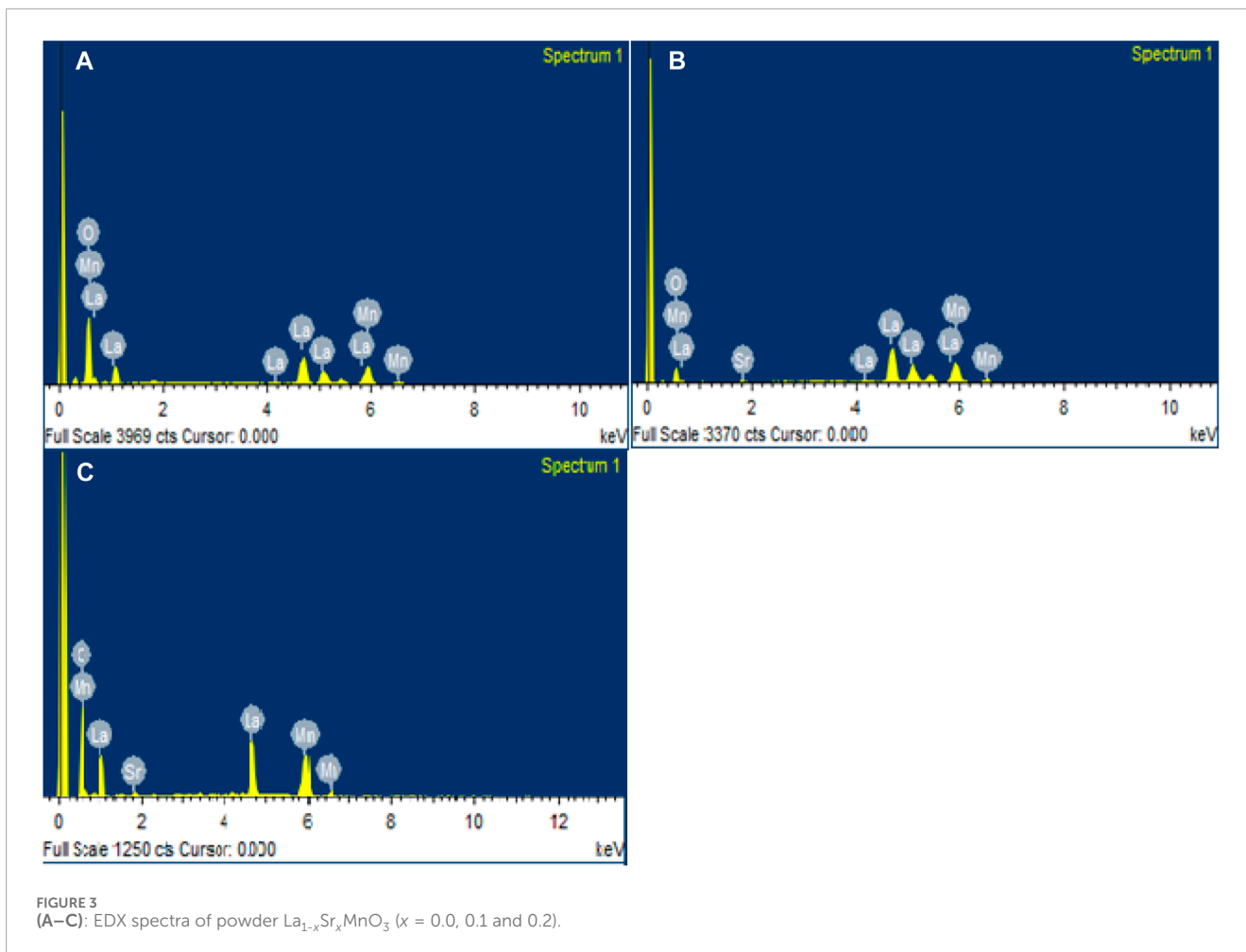
FIGURE 3
(A–C): EDX spectra of powder $La_{1-x}Sr_xMnO_3$ (x = 0.0, 0.1 and 0.2).

TABLE 3 Elemental composition of $La_{1-x}Sr_xMnO_3$ (x = 0.0, 0.1, and 0.2).

$La_{1-x}Sr_xMnO_3$ samples for x =	Weight %					Atomic%				
	La	Sr	Mn	O	Total% (%)	La	Sr	Mn	O	Total% (%)
0.0	46.21	0	19.31	34.48	100	11.72	0	12.38	75.91	100
0.1	65.35	0.38	24.34	9.92	100	30.60	0.29	28.81	40.29	100
0.2	50.72	1.73	23.03	24.52	100	15.63	0.85	17.94	65.59	100

0.2, a notable shift in λ_{max} toward a lower wavelength was detected, corresponding to a blue shift (Gouider Trabelsi et al., 2022).

This variation in absorption edge as a result of different values of x, attributed to the alteration in the optical band gap (E_g) as a function of the diameter of a particle or grain size, can be expressed in terms of the Brass effective model (Hassan et al., 2020).

$$E = E_g^{bulk} + \frac{h^2\Pi^2}{2eR^2} + \left(\frac{1}{m_em_o} + \frac{1}{m_hm_o}\right) - \frac{1.8e}{4\Pi\varepsilon\varepsilon_o}$$
$$- \frac{0.124e^2}{h^2(4\Pi\varepsilon\varepsilon_o)^2}\left(\frac{1}{m_em_o} + \frac{1}{m_hm_o}\right)^{-1} \quad (8)$$

Here, m_e, m_h, and R represent the effective masses of the electrons, holes, and diameter of particle size, respectively, while E_g^{bulk} denotes the bulk energy band gap of the semiconductor material, and ε and ε_0 the relative permittivity of material and permittivity of free space. According to this model, the phenomenon of blue shift can be attributed to an increase in particle size, which leads to a reduction in the excitation energy required for an electron to transition from the valence band to the conduction band. In morphological studies, we have discussed the trend of average particle or grain size, which was increased from 87 to 119 nm and has shown good agreement with obtained values for
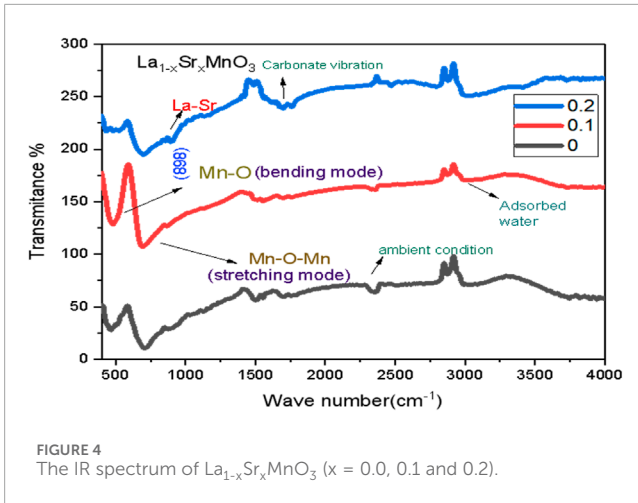
FIGURE 4
The IR spectrum of $La_{1-x}Sr_xMnO_3$ (x = 0.0, 0.1 and 0.2).

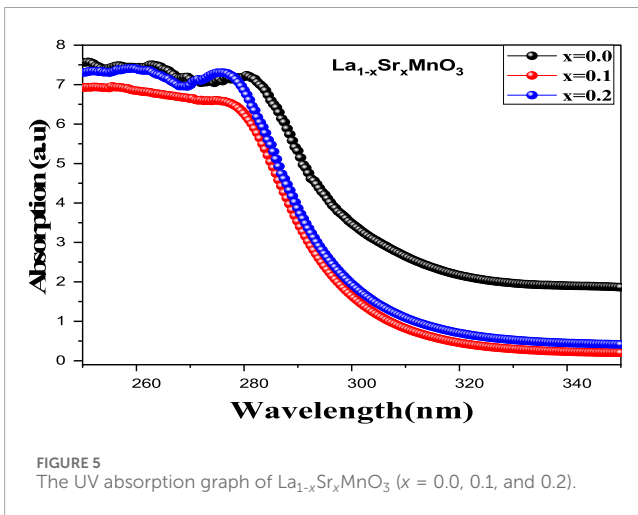**FIGURE 5**
The UV absorption graph of $La_{1-x}Sr_xMnO_3$ (x = 0.0, 0.1, and 0.2).

the optical band gap. Sandhya Suresh et al. (Sandhya et al., 2023) reported in their work that the variation in the optical band gap is due to the interaction of charge transfer between O_2 and Mn^{3+}. The optical band gap (E_g) was estimated using the Wood–Tauc relation (Turky et al., 2017; Zhoua et al., 2023), given as follows:

$$(\alpha h\nu) = K(h\nu - Eg)^{1/m} \qquad (9)$$

where $h\nu$ is the energy of the photon required for transition, K is a constant, and m determines the type of transition, i.e., whether it is direct or indirect; it takes the value of 1/2, 2, 3/2, or 3, representing direct allowed, indirect allowed, direct forbidden, and indirect forbidden transitions. We calculated the optical band gap by first finding the value of α (the absorption coefficient) in the Tauc equation via the Beer–Lambert law, expressed as:

$$\alpha = 2.3003 \times \frac{A}{d}, [24, 55] \qquad (10)$$

where A represents absorbance and d denotes the cuvette's thickness, usually taken as 1 cm. To obtain the values of absorption edges for direct transitions, we plotted the graph $(\alpha h\nu)^2$ vs. E_g, as shown in Figure 6A–C. The optical band gap decreases as Sr^{2+} content rises from 0.0 to 0.2 in the $La_{1-x}Sr_xMnO_3$ system. The values for each

molar ratio of Sr were 4.34 eV, 4.29 eV, and 4.11eV, as listed in Table 4. As predicted based on Eq 8, the grain size increased with a decrease in the energy band gap due to an excess of polaron in the doped LSMO samples, showing good agreement with the quantum size confinement effect (Chandekar et al., 2020b). Ali Omar Turky et al. (Turky et al., 2016) reported that if the band gap is greater than 2 eV, this generally indicates absorption in the UV range. Tuning of the energy band gap (E_g) can be explained by the hooping mechanism involved in the $La_{1-x}Sr_xMnO_3$ system (Turky et al., 2016). The charge transport in the $La^{3+}_{(1-x)} Sr^{2+}_x Mn^{3+}_{(1-x+2\delta)} Mn^{4+}_{(x-2\delta)} O^{2-}_{(3-\delta)}$ chemical formula can be attributed to a change in the Mn^{3+}/Mn^{4+} ratio as a result of d-d transitions as a result of varying the La^{3+}/Sr^{2+} stoichiometric ratio. Ali Omar Turky et al. prepared LSM nanoparticles for values of $x = 0.2, 0.5$, and 0.8 via precipitation (Turky et al., 2016) and citrate precursor (Turky et al., 2017) techniques and found that the optical band gap was increased. Additionally, in 2023, Sandhya Suresh et al. (Sandhya et al., 2023) synthesized a series of LSM nanoparticles for $x = 0.0, 0.3, 0.5, 0.7$ by the combustion method and observed band gap increases with doping. In the current study, we observed that the band gap of LSMO nanoparticles prepared by the precipitation method decreased with the selection of a specific concentration of dopant, strongly confirming the prediction by Andreja Žužić et al. (Žužić et al., 2022) that nanoparticles prepared by this technique have a more conductive nature.

The narrowing of the energy band gap is caused by the small numbers of voids/defects present in a crystal lattice, according to Kamlesh V. Chandekar et al. (Kamlesh et al., 2021a). In the present series of LSMO, results obtained from XRD analysis showed that dislocation density (defects per unit volume) decreased from 0.0044 to 0.0025, correlated with an increase in crystallite size from 15 to 20 nm, as doping concentration of Sr rose from 0.0 to 0.2, which means these stable LSMO nanoparticles have great potential for used as solar cells due to their lower transparency; we calculate their degree of transparency in the upcoming discussion. The elevation of the Fermi level was the result of introducing donor states with Strontium ion content; this also discussed, along with evidence of how much energy is required for the transition to the conduction band and additionally the radius of unoccupied or donor states, which helps us to understand their band structure. Generally, at a low value of x, all states are nondegenerate; whenever we introduce donor states via an extra holding charge carrier, i.e., Sr^{2+}, the effect is to raise the Fermi level—not much in the case of degenerate states (Turky et al., 2017), but near the conduction band, this suppresses the optical band gap. The ionization energy required for the donor atom is given by Eq. 11 with some modifications (Matsuura, 2006):

$$E_d = \frac{13.6}{\varepsilon_r^2} \frac{m_e^*}{m} eV, \qquad (11)$$

where ε_r is the dielectric constant of samples, 13.6 is the ionization energy of the hydrogen atom, and $\left(\frac{m_e^*}{m}\right)$ is the ratio of effective masses of electrons and holes in the material; its value is approximately 0.2, as reported by Kamlesh V. Chandekar et al. (Chandekar et al., 2020b), and the radius of a loosely bound electron of donor orbit can be estimated by the relation $r_d = \varepsilon_r \left(\frac{m}{m_e^*}\right) r_H$, where r_H is the radius of a hydrogen atom (0.53 Å). The results obtained based on these two relations confirmed that the required energy fell (from 0.102 eV to 0.079 eV) as we increased the donor states near

FIGURE 6
(A–C): Energy band gaps for La$_{1-x}$Sr$_x$MnO$_3$ (x = 0.0, 0.1, and 0.2).
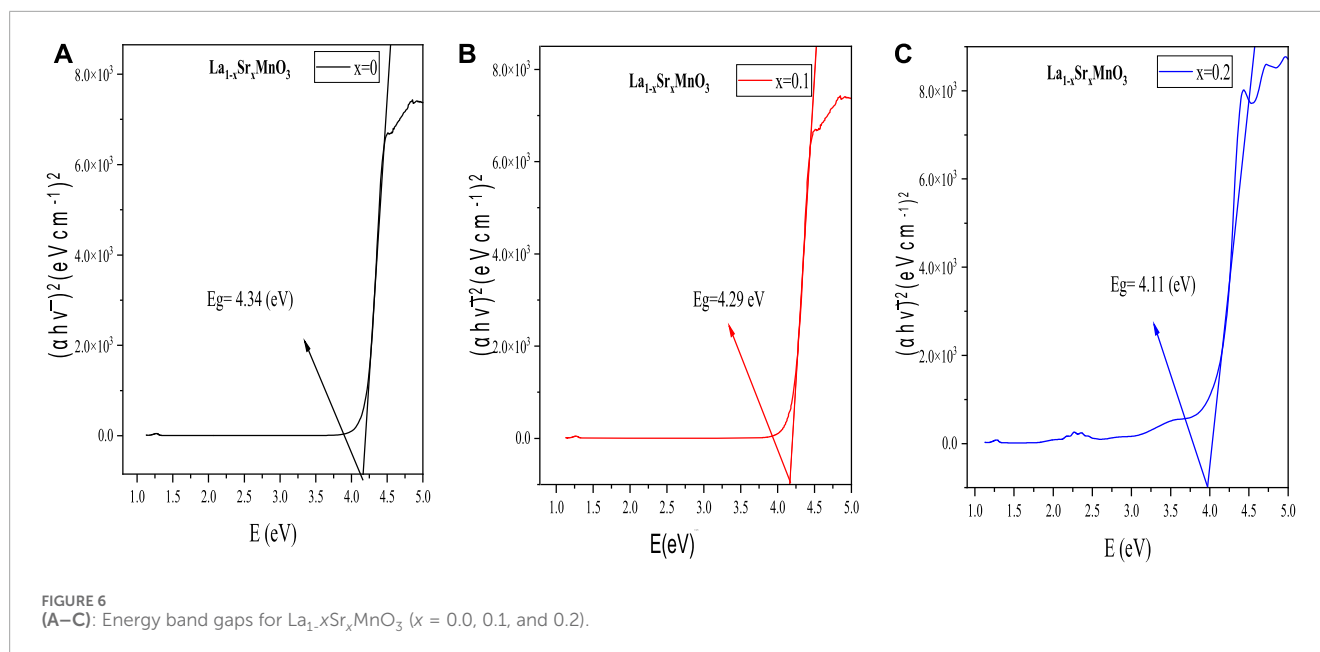
TABLE 4 The optical band gap, refractive index, static dielectric constant, high-frequency dielectric constant, ionization energy, and radius of the donor atom for La$_{1-x}$Sr$_x$MnO$_3$ (x = 0.0, 0.1, and 0.2) nanoparticles.

La$_{1-x}$Sr$_x$MnO$_3$ samples for x =	Optical band gap, E$_g$ (eV)	Refractive index, n (no units)		Static dielectric constant, ε$_0$ (no units)	High-frequency dielectric constant, ε$_α$ (no units)	Ionization energy of donor electrons E$_d$ (eV)	Radius of donor orbit r$_d$ (Å)
		Moss relation	Herve and Vandamme relation				
0.0	4.34	2.163	2.02	5.152	4.678	0.102	13.64
0.1	4.29	2.169	2.03	5.306	4.704	0.096	14.04
0.2	4.11	2.192	2.06	5.862	4.804	0.079	15.52

the edges of the conduction band, and also that the Fermi level radii increased from 13.64 Å to 15.52 Å; all values are displayed in Table 4.

The refractive index is an important parameter in the context of optical measurements that measures the degree of transparency as light passes through the sample material and can be expressed both by Moss and by Herve and Vandamme's relation, as in Eqs 12, 13:

$$E_g n^4 = 95\,eV \tag{12}$$

and

$$n = \sqrt{1 + \left(\frac{A}{Eg + B}\right)^2} \tag{13}$$

Here, A and B are numerical constants with respective ionization energies of 13.6 eV and 3.4 eV. From the data obtained for LSMO nanoparticles based on both relations, it can be noted that there is not much difference in the values of the refractive index. The trend in Table 4 shows that the refractive index increased as we raised the strontium content for x = 0.0 to 0.2. For the higher values of the x, the refractive index decreases, as reported by Sandhya Suresh et al. (Sandhya et al., 2023) in 2023, which means that, at low values, LSMO is more optically dense as compared to higher

values. As explained earlier in XRD analysis, more defects/voids were observed with higher values of Sr in the crystal lattice, which causes more instability. According to Sandhya Suresh et al., (Sandhya et al., 2023), static and high-frequency dielectric constants play a significant role in optoelectronic devices, which can be expressed as:

$$(static\ dielectric\ constant)\,\varepsilon_0 = 18.52 - 3.08E_g \tag{14}$$

$$(high-frequency\ dielectric\ constant)\,\varepsilon_\alpha = n^2 \tag{15}$$

where E$_g$ and n represent the optical band gap and refractive index, respectively; these parameters will be discussed in the following section, and values are additionally presented in Table 4.

3.6 Frequency-dependent dielectric properties

In the preceding section, we have attempted to establish several critical relations correlated with optical behavior, mainly the static and high-frequency dielectric constant. In the present discussion,

we extend this momentum to explain how the electric dipoles of $La_{1-x}Sr_xMnO_3$ for x = 0.0, 0.1, and 0.2 were altered in the presence of varying AC electric fields. To establish the dielectric spectrum, pellets measuring 12.7 mm in diameter with thickness 1.5 mm were made by crushing nanopowder at 10 tons for 10 min, such that these pellets served as electrodes, and samples were taken as the dielectric medium (Shah et al., 2012). An impedance analyzer (1 kHz–2 MHz) was utilized to record frequency-dependent dielectric responses at room temperature, including the dielectric constant (ε'), dielectric loss (ε''), and AC conductivity (δ_{ac}) of $La_{1-x}Sr_xMnO_3$ nanoparticles for x = 0.0, 0.1, and 0.2, as displayed in Figure 7A–C). According to Sandhya Suresh et al. (Sandhya et al., 2023), the behavior of the material in the presence of an external electric field can be expressed in terms of complex dielectric permittivity, defined by ε^* = ε' + ε''. Here, ε' denotes the real part of the dielectric constant, which determines the store of electrical energy. At the same time, ε'' represents the imaginary part of the dielectric constant, which describes the dissipation or loss of energy as heat in a material. The real part of the dielectric may be expressed as in Eq 16:

$$\varepsilon' = \frac{Ct}{\varepsilon_o A} \qquad (16)$$

where t represents the thickness of the sample, ε_o the permittivity of free space, and A the area of the electrode surface (Hizi et al., 2022). The frequency-dependent dielectric constant for all compositions of x is displayed in Figure 7A. In the region of low frequency, a significant increase in the values of the dielectric constant was observed whenever we further increased the frequency; this appears to be independent of frequency. The trend of the dielectric constant as a function of Sr content was consistent with that reported by Sandhya Suresh et al. (Sandhya et al., 2023). The grain boundary effect, interfacial/space charge polarization, charge defects, oxygen vacancies, and the heterogeneous character of the dielectric may all be responsible for the lower frequency high dielectric qualities (Chandekar et al., 2020a; Shkir et al., 2020a; Chandekar et al., 2020b; Shkir et al., 2020b; Kamlesh et al., 2021a; Shkir Mohd et al., 2021; Chandekar et al., 2021b; Gouider Trabelsi et al., 2022; Sandhya et al., 2023). The Maxwell–Wagner model states that dielectric materials are made up of grains with insulating grain boundaries and strongly conducting grains (Kamlesh et al., 2021b; Ben et al., 2023). Charge carriers can easily move between grains and collect at grain borders thanks to the external field (Song et al., 2021). The mobility of charge carriers inside grains and the accumulation of charge at grain borders as a result of the applied field are additional factors that contribute to considerable polarization and a high dielectric constant. Since the dipoles cannot keep up with the applied field, many polarization processes come to an end at higher frequencies. At higher frequency ranges, the end outcome is a drop in the dielectric constant. Mn^{3+} ions shift to Mn^{4+} ions to balance the electrical charge, while La^{3+} ions change to Sr^{2+} ions. The intrinsic dipole is significantly influenced by electron hopping between Mn^{4+} and Mn^{3+}, which enhances the local displacement of charge carriers (Shkir et al., 2020a; Chandekar et al., 2020b; Shkir et al., 2020b; Chandekar et al., 2021b). The dielectric constant decreases along with the concentration of Sr^{2+} ions due to the rapidly moving charge carriers from grains that collect at grain boundaries (Singh and Prasad, 2015; Manohar and Krishnamoorthi, 2017; Manohar et al., 2019). The static dielectric constant is increased,

which means that more charges are introduced on the grain boundaries, enhancing the material's capacity to store electrical energy with an increase in Sr content. In contrast, the more conducting grain in the sample with x = 0.2 indicated the conductive nature of the material, which can be attributed to a reduction in band gap from 4.34 to 4.11 eV, as shown in Table 4. The increase in the dielectric constant can be ascribed to an increase in the particle size, especially in the low-frequency region, and a decrease in the porosity and defects due to the rising Sr content, caused by space charge polarization (Gholizadeh and Banihashemi, 2021; Mojahed et al., 2022; Eghdami and Ahmad, 2023; Tarnack et al., 2023). Due to their extremely high static dielectric constant, these materials serve in storage applications, such as supercapacitors (Sandhya et al., 2023).
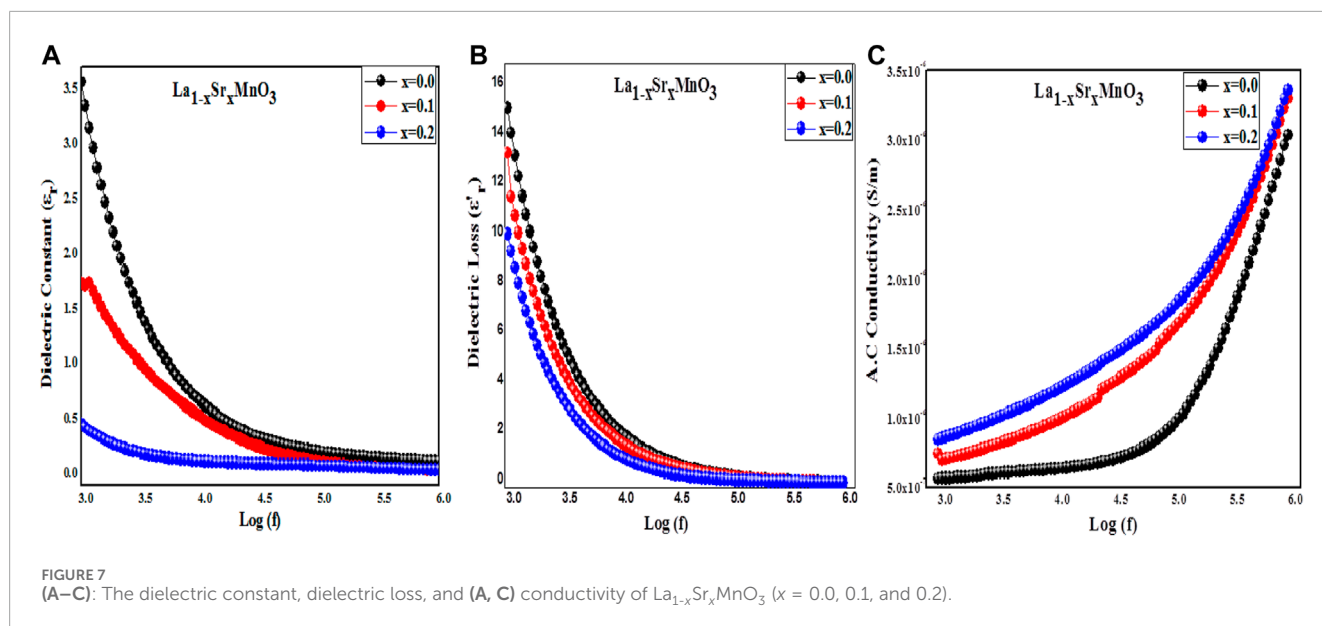
For the frequency range of 1 kHz–2 MHz, Figure 7B displays the frequency response of the dielectric loss for ambient temperature $La_{1-x}Sr_xMnO_3$ nanoparticles (x = 0.0, 0.1, and 0.2), showing the dissipation of energy caused by defects/voids or dislocation density present in the prepared nanoparticles (Kamlesh et al., 2021b). In the region of low frequency, 3.0 log(f) to 5.0 log(f), an increment in the dielectric loss is indicated; this steadily decreases with increasing frequency (>5.0 log(f)), describing the polar nature of the samples. The ε'' vs. f curve can be explained based on the polarization mechanism involved in the material. Typically, high and low values of dielectric loss represent the accumulation of charges across grain boundaries: initially, electric dipoles keep their orientation with the polarity of an AC electric field, corresponding to space charge polarization (SCP), and in the second half they fail to overcome the movement of charge carriers through grain boundaries, resulting in leakage or conduction of current in the samples. Eq. 17 illustrates the connection between polarization and the energy lost by a dielectric medium in an applied field.

$$P = \iiint \varepsilon'' \omega |E|^2 dV, \qquad (17)$$

where E is the electric field vector, ε'' for $La_{1-x}Sr_xMnO_3$ nanoparticles is the dissipation of energy, and ω is the angular frequency (Sandhya et al., 2023). Conduction loss at high frequencies is comparably low due to the low reactance of the applied field; the ability to shift their domain walls, which defect dipoles govern, may be why low-frequency dielectric loss decreases with Sr^{2+} dopant concentration (Sun et al., 2014). The tangent or dielectric loss can be calculated from Eq 18:

$$\tan\delta = \frac{\varepsilon''}{\varepsilon'} \qquad (18)$$

Here ε' and ε'' are the real and imaginary parts of the dielectric (Sandhya et al., 2023). According to Ahmad Gholizadeh et al. (Eghdami and Ahmad, 2023), the energy required to exchange electrons between ions generally represents the constrained motion of domain walls. In the present study, strontium was found to reduce defects, and inhomogeneity had a significant impact on dielectric lost, as discussed earlier with respect to the XRD results, as the molar ratio of Sr^{2+} increases, which reduces the energy required to exchange electrons between Mn^{3+} and Mn^{4+}; this suppresses the optical band gap along with losses in the reported samples. This variation can also be explained in terms of particle size (Mojahed et al., 2022; Eghdami and Ahmad, 2023), with less resistive grains being offered by relatively larger particle sizes; in

FIGURE 7
(A–C): The dielectric constant, dielectric loss, and **(A, C)** conductivity of $La_{1-x}Sr_xMnO_3$ (x = 0.0, 0.1, and 0.2).

the present scenario, particle size increased by means of Sr doping led to a decrease in defects/inhomogeneity, optical band gap, and dielectric loss, which makes these materials the best candidates for energy storage and photovoltaic devices.

Figure 7C shows the AC conductivity of $La_{1-x}Sr_xMnO_3$ (x = 0.0, 0.1, and 0.2) perovskite nanoparticles as a function of frequency. The presence of frequency-dependent and -independent regions observed in this curve is due to the polar nature of dielectrics. In the region of low (3.0 log(f) to 4.0 log(f)) frequency, the fact that AC conductivity is lower may be attributed to high resistive grain boundaries that resist tunneling of charge carriers. Ahmad Gholizadeh et al. (Ahmad and Beyranvand, 2020) reported in their work that interfacial polarization is the reason for this low-conductivity behavior. Similarly, at high (>4.0 log(f)) frequencies, a significant increase in the conductivity was observed as a result of the smaller numbers of grains present in the reported samples (Amini and Ahmad, 2020). A notable relaxation was observed in pure samples, which might be due to the availability of fewer charge carriers as compared to doped samples, which exhibited relatively more conduction. The AC conductivity of the sample can be related to leakage current or angular frequency, as follows:

$$AC\,Conductivity = \varepsilon'' \varepsilon_o \omega \qquad (19)$$

where ε'' and ω represent the dielectric loss and may be referred to as leakage current and angular frequency, respectively.

The flat response of the sample in the low-frequency range may be attributed to the DC component of conductivity. Low-frequency ion accumulation and low conductivity are the results of the electric field's delayed periodic reversal. Johnscher's universal power law (Chandekar et al., 2020b) provides the clearest description of frequency-dependent AC conductivity. The use of Sr^{2+} as a dopant plays a vital role in enhancing the AC conductivity of LSMO nanocrystals by introducing donor states with an excess of polarons; these reduce the defects/inhomogeneity and also the porosity of the material (Sandhya et al., 2023). Similarly, Ahmad Gholizadeh et al. (Amini

and Ahmad, 2020) utilized different dopants in $MFe_{12}O_{19}$ (M = Ba, Pb, Sr) and examined frequency-dependent AC conductivity; they found that the strontium-doped sample exhibited higher conductivity due to highly conductive grains present in the sample. Eq. 20, which reflects the conduction process in $La_{1-x}Sr_xMnO_3$, attributes the defects in the host lattice caused by the partial replacement of the Sr^{2+} ion to charge transport, with hopping charged carriers over disordered arrangements:

$$\delta_{ac} = \delta_{dc}\left[1 + \left(\frac{\omega}{\omega_H}\right)^s\right], \qquad (20)$$

where ω_H represents hopping frequency and s is is an exponent of frequency that can be determined based on the δ_{ac} vs. f plot given in Figure 7C by fitting of linear sections. Bulk resistance and capacitance are the main causes of the tendency to higher frequencies and the effects of high-frequency capacitance (Turky et al., 2016). One study has reported that less energy is required for the hooping of electrons between two ions in a region of high frequency (Eghdami and Ahmad, 2023). In the $La_{1-x}Sr_xMnO_3$ system, the higher Sr^{2+}/La^{3+} ratio offered more vacancies due to the interaction of charge carriers in O^{2-} and Mn^{3+}, leading to an increase in electronic charge transport across smaller grain boundaries, which can be attributed to larger particle sizes. The hooping mechanism determines the true essence of AC conductivity in the material because the mobility of carriers in the doped samples enables tunneling through such small grains as a result of the reduced amount of energy required for exchange between Mn^{3+} and Mn^{4+} ions. All the findings of the present study support the frequency dependence response of AC conductivity, mainly as a result of the optical band gap, structural imperfections, and particle size, indicating that this material is best used in solid oxide fuel cells and photovoltaic devices.

4 Conclusion

1. In this study, optoelectrical properties as a function of different ($0.0 \leq x \leq 0.2$) concentrations of Sr^{2+} in a host lattice $La_{1-x}Sr_xMnO_3$ have been investigated. All reported samples of LSMO nanoparticles were successfully synthesized via the co-precipitation method, with no extra phases or impurities observed in XRD, FESEM, or EDX spectra.

2. Structural studies revealed a rhombohedral ($R\bar{3}c - \text{space group}$) crystal structure for all prepared samples of LSMO nanoparticles, with crystallite size in the range of 15 to 20 nm. It was observed that Sr enhances crystallinity by decreasing the dislocation density from 0.0044 to 0.0025. A slight increase in the unit cell volume for the 0.1 sample was attributed to the micro-strain of approximately 3.091 exerted by Sr^{2+} (1.44 Å) on the host lattice. X-ray density and specific surface area were decreased by up to 6.55 (g/cm^3) and 45.80 (cm^2/g) respectively.

3. Morphological and compositional analysis showed that the prepared samples had polygonal or hexagonal-like structures, with average particle or grain size estimated from SEM images in the range of 87–119 nm. Based on the EDX spectra, the purity or molar ratio of each composition in the compound was confirmed; additionally, bonds in the fingerprint region of 400–1,500 cm^{-1} were confirmed by FTIR analysis.

4. The optoelectrical properties of un-doped and Sr-doped samples indicated that the elevation of donor states near the conduction band suppressed the optical band gap from 4.34 eV to 4.11 eV, which was correlated with the refractive index. Moss's relation showed increases in refractive index from 2.163 to 2.192, which means that the samples became more optically dense with higher Sr content. The static and frequency-dependent dielectric constant increased with an increase in Sr content, which means that the reported samples have the potential to serve in energy storage devices and high-frequency transmission cables due to their minimal dielectric losses. Finally, AC conductivity increased with an excess of polarons in the heavy-doped sample.

Based on the above points, we conclude that LSMO nanoparticles with low Sr content are more stable and represent a promising material for application in solid oxide fuel cells (SOFCs) and electronic storage devices.

Data availability statement

The original contributions presented in the study are included in the article/Supplementary material, further inquiries can be directed to the corresponding authors.

Author contributions

AA: Conceptualization, Data curation, Formal Analysis, Investigation, Methodology, Project administration, Resources, Software, Validation, Writing–original draft, Writing–review and editing. WS: Conceptualization, Methodology, Supervision, Writing–review and editing, Data curation, Formal Analysis, Investigation. ZU: Formal Analysis, Investigation, Writing–review and editing. SM: Conceptualization, Data curation, Investigation, Writing–review and editing. MR: Formal Analysis, Investigation, Methodology, Writing–review and editing. SA: Writing–review and editing, Data curation, Methodology, Validation, Visualization, Software. NI: Investigation, Writing–review and editing. HA: Writing–review and editing, Data curation, Validation, Visualization, Software.

Funding

Conflict of interest

The authors declare that the research was conducted in the absence of any commercial or financial relationships that could be construed as a potential conflict of interest.

Publisher's note

All claims expressed in this article are solely those of the authors and do not necessarily represent those of their affiliated organizations, or those of the publisher, the editors and the reviewers. Any product that may be evaluated in this article, or claim that may be made by its manufacturer, is not guaranteed or endorsed by the publisher.

References

Afify, M. S., El Faham, M. M., Eldemerdash, U., El Rouby, W. M., and El-Dek, S. (2021). Room temperature ferromagnetism in Ag doped LaMnO3 nanoparticles. *J. alloys Compd.* 861 (2021), 158570. doi:10.1016/j.jallcom.2020.158570

Ahmad, G., and Beyranvand, M. (2020). Investigation on the structural, magnetic, dielectric and impedance analysis of Mg0.3-xBaxCu0.2Zn0.5Fe2O4 nanoparticles. *Phys. B* 584, 412079. doi:10.1016/j.physb.2020.412079

Ali, A., Shah, W. H., Safeen, A., Ali, L., Tufail, M., Ullah, Z., et al. (2023a). Effect of Ca doping on the arbitrary canting of magnetic exchange interactions in La1-xCaxMnO3 nanoparticles. *Front. Mater.* 10 (2023), 1117793. doi:10.3389/fmats.2023.1117793

Ali, A. H., Ahmed, A. M., Abdelhamied, M. M., Abdel-Khaliek, A. A., Khalik, S. A. E., Abass, S. M., et al. (2023b). *Synthesis of lead-free Cu/CuFeO 2/CZTS thin film as a novel photocatalytic hydrogen generator from wastewater and solar cell applications.* doi:10.21203/rs.3.rs-3304698/v1

Amini, M., and Ahmad, G. (2020). Shape control and associated magnetic and dielectric properties of MFe12O19 (M = Ba, Pb, Sr) hexaferrites. *J. Phys. Chem. Solids* 147, 109660. doi:10.1016/j.jpcs.2020.109660

Arshad, M., Huiling, D., Sufyan, J. M., Maqsood, A., Ashraf, I., Hussain, S., et al. (2020). Fabrication, structure, and frequency-dependent electrical and dielectric properties of Sr doped BaTiO3 ceramics. *Ceram. Int.* 46 (2), 2238–2246. doi:10.1016/j.ceramint.2019.09.208

Assoudi, N., Hzez, W., Dhahri, R., Walha, I., Rahmouni, H., Khirouni, K., et al. (2018). Physical properties of Ag/Ca doped Lantanium manganite. *J. Mater. Sci. Mater. Electron.* 29, 20113–20121. doi:10.1007/s10854-018-0143-5

Ben, A., Alkallas, F. H., Chandekar, K. V., Kumar, A., Ubaidullah, M., Shkir, M., et al. (2023). Facile low temperature development of Ag-doped PbS nanoparticles for optoelectronic applications. *Mater. Chem. Phys.* 297, 127299. doi:10.1016/j.matchemphys.2023.127299

Chandekar, K. V., Khan, A., Alshahrani, T., Shkir, M., Kumar, A., El-Toni, A. M., et al. (2020a). Novel rare earth Dy doping impact on physical properties of PbI2 nanostructures synthesized by microwave route for optoelectronics. *Mater. Charact.* 170, 110688. doi:10.1016/j.matchar.2020.110688

Chandekar, K. V., Shkir, M., Khan, A., and AlFaify, S. (2020b). An in-depth study on physical properties of facilely synthesized Dy@CdS NPs through microwave route for optoelectronic technology. *Mater. Sci. Semicond. Process.* 118, 105184. doi:10.1016/j.mssp.2020.105184

Chandekar, K. V., Shkir, M., Khan, A., Sayed, M., Alotaibi, N., Alshahrani, T., et al. (2021b). Significant and systematic impact of yttrium doping on physical properties of nickel oxide nanoparticles for optoelectronics applications. *J. Mater. Res. Technol.* 15, 2584–2600. e260. doi:10.1016/j.jmrt.2021.09.072

Eghdami, F., and Ahmad, G. (2023). A correlation between microstructural and impedance properties of MnFe2-Co O4 nanoparticles. *Phys. B* 650, 414551. doi:10.1016/j.physb.2022.414551

Flores-Lasluisa, J. X., Huerta, F., Cazorla-Amorós, D., and Morallón, E. (2022). Manganese oxides/LaMnO3 perovskite materials and their application in the oxygen reduction reaction. *Energy* 247 (2022), 123456. doi:10.1016/j.energy.2022.123456

Gholizadeh, A., and Banihashemi, V. (2021). *Effects of Ca–Gd co-substitution on the structural, magnetic, and dielectric properties of M-type strontium hexaferrit.* doi:10.1111/jace.1919

Gholizadeh, A., and Tajabor, N. (2010). Influence of N2- and Ar-ambient annealing on the physical properties of SnO2:Co transparent conducting films. *Mater. Sci. Semicond. process.* 13 (3), 162–169. doi:10.1016/j.mssp.2010.10.004

Gouider Trabelsi, A. B., Chandekar, K. V., Alkallas, F., Ashraf, I., Hakami, J., Shkir, M., et al. (2022). A comprehensive study on Co-doped CdS nanostructured films fit for optoelectronic applications. *J. Mater. Res. Technol.* 21, 3982–4001. e4001. doi:10.1016/j.jmrt.2022.11.002

Hassan, A. A. S., Khan, W., Husain, S., Dhiman, P., and Singh, M. (2020). Investigation of structural, optical, electrical, and magnetic properties of Fe-doped La0. 7Sr0. 3MnO3 manganites. *Int. J. Appl. Ceram. Technol.* 17 (5), 2430–2438. doi:10.1111/ijac.13540

Hernández, E., Sagredo, V., and Delgado, G. E. (2015). Synthesis and magnetic characterization of LaMnO3 nanoparticles. *Rev. Mex. física* 61 (3), 166–169.

Hizi, W., Gassoumi, M., Rahmouni, H., Guesmi, A., Ben Hamadi, N., and Dhahri, E. (2022). Effect of sintering temperature and polarization on the dielectric and electrical properties of La0. 9Sr0. 1MnO3 manganite in alternating current. *Materials* 15 (10), 3683. doi:10.3390/ma15103683

Hu, J., Zhang, L., Lu, B., Wang, X., and Huang, H. (2019). LaMnO3 nanoparticles supported on N doped porous carbon as efficient photocatalyst. *Vacuum* 159, 59–68. doi:10.1016/j.vacuum.2018.10.021

Jadhav, S., Nikam, D., Khot, V., Mali, S., Hong, C., and Pawar, S. (2015). PVA and PEG functionalised LSMO nanoparticles for magnetic fluid hyperthermia application. *Mater. Charact.* 102, 209–220. doi:10.1016/j.matchar.2015.03.001

Jheng-Yun, L., Hong-Kai, C., Cheng-Che, H., and Jian-Zhang, C. (2023). LiMn2O4 Li-ion hybrid supercapacitors processed by nitrogen atmospheric-pressure plasma jet. *Ceram. Int.* 49, 11067–11107. doi:10.1016/j.ceramint.2022.11.303

Kamlesh, V. C., Alshahrani, T., Ben Gouider Trabelsi, A., Alkallas, F. H., Shkir, M., and AlFaify, S. (2021a). Novel rare earth yttrium doping effect on physical properties of PbS nanostructures: facile synthesis and characterization. *J. Mater Sci.* 56, 4763–4781. doi:10.1007/s10853-020-05539-w

Kamlesh, V. C., Shkir, M., Palanivel, B., Ahmad, Z., Algarni, H., and AlFaify, S. (2021b). Comparative study of Pr-doped and undoped PbS nanostructures facilely synthesized for optoelectronic applications. *Solid State Sci.* 122, 106773. doi:10.1016/j.solidstatesciences.2021.106773

Li, C., Yu, Z., Liu, H., and Chen, K. (2018). High surface area LaMnO3 nanoparticles enhancing electrochemical catalytic activity for rechargeable lithium-air batteries. *J. Phys. Chem. Solids* 113, 151–156. doi:10.1016/j.jpcs.2017.10.039

Manohar, A., and Krishnamoorthi, C. (2017). Structural, optical, dielectric and magnetic properties of CaFe2O4 nanocrystals prepared by solvothermal reflux method. *J. Alloys Compd.* 722, 818–827. doi:10.1016/j.jallcom.2017.06.145

Manohar, A., Krishnamoorthi, C., Naidu, K. C. B., and Pavithra, C. (2019). Dielectric, magnetic hyperthermia, and photocatalytic properties of ZnFe 2 O 4 nanoparticles synthesized by solvothermal reflux method. *Appl. Phys. A* 125, 477–510. doi:10.1007/s00339-019-2760-0

Matsuura, H. (2006). Influence of excited states of a deep substitutional dopant on majority-carrier concentration in semiconductors. *Phys. Rev. B* 74, 245216. doi:10.1103/PhysRevB.74.245216

McBride, K., Cook, J., Gray, S., Felton, S., Stella, L., and Poulidi, D. (2016). Evaluation of La 1– x Sr x MnO 3 (0≤ x< 0.4) synthesised via a modified sol–gel method as mediators for magnetic fluid hyperthermia. *CrystEngComm* 18 (3), 407–416. doi:10.1039/c5ce01890k

Miao, He, Wu, X., Chen, B., Wang, Q., Wang, F., Wang, J., et al. (2020). A-site deficient/excessive effects of LaMnO3 perovskite as bifunctional oxygen catalyst for zinc-air batteries. *Electrochimica Acta* 333, 135566. doi:10.1016/j.electacta.2019.135566

Mleiki, A., Khlifi, A., Rahmouni, H., Guermazi, N., Khirouni, K., Hlil, E., et al. (2020). Magnetic and dielectric properties of Ba-lacunar La0. 5Eu0. 2Ba0. 3MnO3 manganites synthesized using sol-gel method under different sintering temperatures. *J. Magnetism Magnetic Mater.* 502, 166571. doi:10.1016/j.jmmm.2020.166571

Mohanty, D., Mallick, P., Biswal, S., Behera, B., Mohapatra, R. K., Behera, A., et al. (2020b). Investigation of structural, dielectric and electrical properties of ZnFe2O4 composite. *Mater. Today Proc.* 33, 4971–4975. doi:10.1016/j.matpr.2020.02.827

Mohanty, D., Satpathy, S. K., Behera, B., and Mohapatra, R. K. (2020a). Dielectric and frequency dependent transport properties in magnesium doped CuFe2O4 composite. *Mater. Today Proc.* 33 (2020), 5226–5231. doi:10.1016/j.matpr.2020.02.944

Mojahed, M., Dizaji, H. R., and Gholizadeh, A. (2022). Structural, magnetic, and dielectric properties of Ni/Zn co-substituted CuFe2O4 nanoparticles. *Phys. B* 646, 414337. doi:10.1016/j.physb.2022.414337

Naseem Siddique, M., Ahmed, A., and Tripathi, P. (2019). Enhanced optical properties of pure and Sr doped NiO nanostructures: a comprehensive study. *Optik* 185, 599–608. doi:10.1016/j.ijleo.2019.03.150

Özkan, Ç., Türk, A., and Celik, E. (2021). Synthesis and characterizations of LaMnO3 perovskite powders using sol–gel method. *J. Mater. Sci. Mater. Electron.* 32 (11), 15544–15562. doi:10.1007/s10854-021-06104-0

Sandhya, S., Vindhya, P. S., Devika, S., and Kavitha, V. T. (2023). structural, optical and dielectric properties of nanostructured La1– xSrxMnO3 perovskites. *Mater. Today Commun.* 36, 106657. doi:10.1016/j.mtcomm.2023.106657

Shafi, P. M., Joseph, N., Thirumurugan, A., and Bose, A. C. (2018). Enhanced electrochemical performances of agglomeration-free LaMnO3 perovskite nanoparticles and achieving high energy and power densities with symmetric supercapacitor design. *Chem. Eng. J.* 338, 147–156. doi:10.1016/j.cej.2018.01.022

Shah, W. H., Safeen, K., and Rehman, G. (2012). Effects of divalent alkaline earth ions on the magnetic and transport features of La0. 65A0. 35Mn0. 95Fe0. 05O3 (A= Ca, Sr, Pb, Ba) compounds. *Curr. Appl. Phys.* 12 (3), 742–747. doi:10.1016/j.cap.2011.10.015

Shkir, M., Chandekar, K. V., Alshahrani, T., Kumar, A., Khan, A., and AlFaify, S. (2020b). An impact of La doping content on key physical properties of PbS spherical nanoparticles facilely synthesized via low temperature chemical route. *Eur. Phys. J. Plus* 135, 816. doi:10.1140/epjp/s13360-020-00740-x

Shkir, M., Chandekar, K. V., Khan, A., Alshahrani, T., Mohamed El-Toni, A., Sayed, M., et al. (2021a). Tailoring the structure-morphology-vibrational-optical-dielectric and electrical characteristics of Ce@NiO NPs produced by facile combustion route for optoelectronics. *Mater. Sci. Semicond. Process.* 126, 105647. doi:10.1016/j.mssp.2020.105647

Shkir, M., Khan, Z. R., Chandekar, K. V., Alshahrani, T., Kumar, A., and AlFaify, S. (2020a). A facile microwave synthesis of Cr-doped CdS QDs and investigation of their physical properties for optoelectronic applications. *Appl. Nanosci.* 10, 3973–3985. doi:10.1007/s13204-020-01505-9

Singh, K. P., and Prasad, A. (2015). Effects of Sr2+ doping on the electrical properties of (Bi0. 5Na0. 5) 0.94 Ba0. 06TiO3 ceramics. *Process. Appl. Ceram.* 9 (1), 33–42. doi:10.2298/pac1501033s

Solopan, S. O., V'yunov, O., Belous, A., Polek, T., and Tovstolytkin, A. (2012). Effect of nanoparticles agglomeration on electrical properties of La1– xAxMnO3 (A= Sr, Ba) nanopowder and ceramic solid solutions. *Solid state Sci.* 14 (4), 501–505. doi:10.1016/j.solidstatesciences.2012.01.030

Song, G., Zhang, Y., Li, S., Yang, J., Bai, W., and Tang, X. (2021). Dielectric relaxation behavior of BTO/LSMO heterojunction. *Nanomaterials* 11 (5), 1109. doi:10.3390/nano11051109

Sun, X., Li, X., Hou, S., Huang, C., Zou, J., Li, M., et al. (2014). The effect of Mg doping on the dielectric and tunable properties of Pb0. 3Sr0. 7TiO3 thin films

prepared by sol–gel method. *Appl. Phys. A* 114 (3), 777–783. doi:10.1007/s00339-013-7645-z

Tarnack, M., Czaderna-Lekka, A., Wojnarowska, Z., Kaminski, K., and Paluch, M. (2023). Nature of dielectric response of phenyl alcohols. *J. Phys. Chem. B* 127, 6191–6196. doi:10.1021/acs.jpcb.3c02335

Turky, A. O., and Kandil, A. T. (2013). Optical and electrical properties of Ba1−x Sr x TiO3 nanopowders at different Sr2+ ion content. *J. Mater Sci. Mater Electron* 24, 3284–3291. doi:10.1007/s10854-013-1244-9

Turky, A. O., Rashad, M. M., Hassan, A. M., Elnaggar, E. M., and Bechelany, M. (2016). Tailoring optical, magnetic and electric behavior of lanthanum strontium manganite La 1− x Sr x MnO 3 (LSM) nanopowders prepared via a co-precipitation method with different Sr 2+ ion contents. *RSC Adv.* 6 (22), 17980–17986. doi:10.1039/c5ra27461c

Turky, A. O., Rashad, M. M., Hassan, A. M., Elnaggar, E. M., and Bechelany, M. (2017). Optical, electrical and magnetic properties of lanthanum strontium manganite La 1− x Sr x MnO 3 synthesized through the citrate combustion method. *Phys. Chem. Chem. Phys.* 19 (9), 6878–6886. doi:10.1039/c6cp07333f

Wang, H., Ling, F., Li, Y., Wu, D., Qi, L., Liang, Z., et al. (2022). Effect of V doping on the electrical transport and magnetoresistance properties of La0. 825Sr0. 175MnO3 ceramics. *J. Sol-Gel Sci. Technol.* 103 (3), 799–806. doi:10.1007/s10971-022-05870-5

Yan, Z., Liu, H., Hao, Z., Meng, Yu, Chen, X., and Chen, J. (2020). Electrodeposition of (hydro) oxides for an oxygen evolution electrode. *Chem. Sci.* 11, 10614–10625. doi:10.1039/d0sc01532f

Zhong, W., Au, C.-T., and Du, Y.-W. (2013). Review of magnetocaloric effect in perovskite-type oxides. *Chin. Phys. B* 22, 057501, 057501. doi:10.1088/1674-1056/22/5/057501

Zhoua, H., Kea, J., Xua, D., and Liub, J. (2023). MnWO4 nanorods embedded into amorphous MoS microsheets in 2D/1D MoS/MnWO4 S–scheme heterojunction for visible-light photocatalytic water oxidation. *J. Mater. Sci. Technol.* 136, 169–179. doi:10.1016/j.jmst.2022.07.021

Žužić, A., Ressler, A., Šantić, A., Macan, J., and Gajović, A. (2022). The effect of synthesis method on oxygen nonstoichiometry and electrical conductivity of Sr-doped lanthanum manganites. *J. Alloys Compd.* 907 (2022), 164456. doi:10.1016/j.jallcom.2022.164456